NASA/TM—2018-219883

Effect of Thin-Film Adhesives on Mode I Interlaminar Fracture Toughness in Carbon Fiber Composites With Shape Memory Alloy Inserts

Derek J. Quade
Glenn Research Center, Cleveland, Ohio

Sadhan C. Jana, Gregory N. Morscher, and Manigandan Kannan
The University of Akron, Akron, Ohio

Linda S. McCorkle
Ohio Aerospace Institute, Brook Park, Ohio

June 2018

NASA STI Program . . . in Profile

Since its founding, NASA has been dedicated to the advancement of aeronautics and space science. The NASA Scientific and Technical Information (STI) Program plays a key part in helping NASA maintain this important role.

The NASA STI Program operates under the auspices of the Agency Chief Information Officer. It collects, organizes, provides for archiving, and disseminates NASA's STI. The NASA STI Program provides access to the NASA Technical Report Server—Registered (NTRS Reg) and NASA Technical Report Server—Public (NTRS) thus providing one of the largest collections of aeronautical and space science STI in the world. Results are published in both non-NASA channels and by NASA in the NASA STI Report Series, which includes the following report types:

- TECHNICAL PUBLICATION. Reports of completed research or a major significant phase of research that present the results of NASA programs and include extensive data or theoretical analysis. Includes compilations of significant scientific and technical data and information deemed to be of continuing reference value. NASA counter-part of peer-reviewed formal professional papers, but has less stringent limitations on manuscript length and extent of graphic presentations.

- TECHNICAL MEMORANDUM. Scientific and technical findings that are preliminary or of specialized interest, e.g., "quick-release" reports, working papers, and bibliographies that contain minimal annotation. Does not contain extensive analysis.

- CONTRACTOR REPORT. Scientific and technical findings by NASA-sponsored contractors and grantees.

- CONFERENCE PUBLICATION. Collected papers from scientific and technical conferences, symposia, seminars, or other meetings sponsored or co-sponsored by NASA.

- SPECIAL PUBLICATION. Scientific, technical, or historical information from NASA programs, projects, and missions, often concerned with subjects having substantial public interest.

- TECHNICAL TRANSLATION. English-language translations of foreign scientific and technical material pertinent to NASA's mission.

For more information about the NASA STI program, see the following:

- Access the NASA STI program home page at http://www.sti.nasa.gov

- E-mail your question to help@sti.nasa.gov

- Fax your question to the NASA STI Information Desk at 757-864-6500

- Telephone the NASA STI Information Desk at 757-864-9658

- Write to:
  NASA STI Program
  Mail Stop 148
  NASA Langley Research Center
  Hampton, VA 23681-2199

NASA/TM—2018-219883

Effect of Thin-Film Adhesives on Mode I Interlaminar Fracture Toughness in Carbon Fiber Composites With Shape Memory Alloy Inserts

Derek J. Quade
Glenn Research Center, Cleveland, Ohio

Sadhan C. Jana, Gregory N. Morscher, and Manigandan Kannan
The University of Akron, Akron, Ohio

Linda S. McCorkle
Ohio Aerospace Institute, Brook Park, Ohio

National Aeronautics and
Space Administration

Glenn Research Center
Cleveland, Ohio 44135

June 2018

Level of Review: This material has been technically reviewed by technical management.

Available from

Effect of Thin-Film Adhesives on Mode I Interlaminar Fracture Toughness in Carbon Fiber Composites With Shape Memory Alloy Inserts

Derek J. Quade
National Aeronautics and Space Administration
Glenn Research Center
Cleveland, Ohio 44135

Sadhan C. Jana, Gregory N. Morscher, and Manigandan Kannan
The University of Akron
Akron, Ohio 44325

Linda S. McCorkle
Ohio Aerospace Institute
Brook Park, Ohio 44142

Summary

A single sheet of NiTi shape memory alloy (SMA) was introduced within a unidirectional HexPly® 8552/IM7 (Hexcel®) polymer matrix composite (PMC) panel in conjunction with multiple thin-film adhesives to promote the interfacial bond strength between the SMA and PMC. A double cantilever beam (DCB) test was performed in accordance with the ASTM D5528 method for evaluation of Mode I interlaminar fracture toughness of unidirectional fiber-reinforced PMCs. The modal acoustic emissions (MAEs) were monitored during testing with two acoustic sensors attached to the specimens. The composite panels were subjected to a C-scan before testing and examined using optical and scanning electron microscopy (SEM) techniques after part failure. The data were used in conjunction with modified beam theory (MBT), the compliance calibration (CC) method, and the modified compliance calibration (MCC) method. The Mode I interlaminar toughness (G_{IC}) values for control specimens were higher than previously reported and are attributed to extensive fiber bridging during testing. The presence of adhesives with SMA inserts stabilized crack propagation during DCB testing. The results reveal a new phenomenon of SMA bridging, whereby crack propagation would switch from one side of the SMA insert to the other, thus increasing the load and G_{IC} values of specimens containing SMA.

1.0 Introduction

Shape memory alloys (SMAs) embedded within polymers have opened a new area of interest as a hybrid actuator due to their ability to change shape. A variety of different studies have looked at shape change within constrained polymers. Characterization of NiTi wires and NiTi strips within a variety of composites has received a fair amount of attention. Examples of this research include debonding analysis of NiTi wires within carbon fiber (Ref. 1) and epoxy (Refs. 2 to 4) systems along with thermomechanical analysis of NiTi strips in epoxy systems (Refs. 4, 5 (p. 343), and 6). NiTi fabrication within composites has also generated research into the application of SMAs in chevrons (Ref. 7) and stress analysis based on bending (Ref. 8) and buckling (Ref. 9) as well as modeling SMA debonding within a composite (Ref. 10). SMAs embedded within polymers have also opened a new area of interest based on hybrid actuators (Refs. 11 to 13) in view of their ability to change shape upon the application of heat. However, SMAs and polymers are dissimilar materials, and in order to advance these material systems properly to other applications, further investigation is required to fully understand and to optimize the bonds between these dissimilar materials.

As is apparent, the actuation function is derived from the SMA itself. The SMA is able to generate large amounts of stress when constrained through reversible, thermoelastic martensitic transitions of the crystalline structure (Ref. 14). Austenitic crystals shift to a variety of martensitic structures during times of loading or heating. This shift is directly responsible for the aforementioned stresses generated when constrained, as is the case when embedded within a composite (Ref. 15). The bending and flexing that occur within an SMA-polymer matrix composite (PMC) actuator system depend highly on the interlaminar strength between the two dissimilar materials.

Several prior investigations focused on the modeling of the actuator stresses (Refs. 6 and 11), enhancement of the SMA–PMC bonding (Refs. 1 to 4 and 10), and fabrication of an actuator system (Refs. 6 to 8, 10, and 12). A majority of prior research used optically clear systems (Refs. 2 to 12), whereby glass or aramid fibers were combined with optically clear resins. The optical clarity of the systems allowed monitoring of the strains and debonding using optical methods, such as Raman spectroscopy. Very few studies have looked at the interactions between SMAs and PMCs in systems that are not optically clear, typically involving carbon fiber reinforced polymer (CFRP) composites (Refs. 1, 16, and 17).

The goals of this research are to assess the effects of the thin-film adhesives and to examine the interlaminar strength between an SMA and PMC in an actuator. A series of four 22-ply unidirectional composite panels were fabricated for the purpose. In addition to a control PMC panel with no SMA, three panels that included a central SMA sheet were manufactured. Two of the three SMA panels included additional thin-film adhesives placed between the SMA sheet and the PMC adjacent plies to achieve better interfacial bonding. The panels were subjected to double cantilever beam (DCB) testing in accordance with the ASTM D5528 test method for Mode I interlaminar fracture toughness of unidirectional fiber-reinforced PMCs (Ref. 18). Two acoustic sensors were attached to the specimens for monitoring of modal acoustic emissions (MAEs). Acoustic Emission (AE) was used for detection of debonding in the specimens during interlaminar failure. We believe this method yields better results than the visual methods of inspection of failed specimens after mechanical testing (Refs. 1 to 4 and 9 to 11).

2.0   Experimental Methods

2.1   Polymer Matrix Composite (PMC) Panel Layup

The PMC panel layup was based on specifications provided by the ASTM D5528 test method (Ref. 18). PMC panels with an average thickness of 3.56 mm were fabricated by organizing 22 plies with 0° unidirectional fiber orientation. Figure 1 schematically shows this structure. Of these, 11 plies of materials were put on either side of a single sheet of SMA material. A nonstick insert was placed between the SMA and the PMC (over a portion of the interface) to serve as a precrack in the DCB test specimens. Control panels were fabricated with no SMA at all, or with no adhesives, but these control panels still contained the precrack as discussed above to remain compatible with the DCB testing.

2.2   Materials and Fabrication

Flat, annealed NiTi sheets were supplied by Johnson Matthey, measuring 457 mm long, 101.6 mm wide, and 0.127 mm thick. The SMA sheets were cut into rectangular specimens 152.4 mm long by 101.6 mm wide. The SMA specimens were wiped with acetone and dried before insertion in the PMC. The PMC used was a HexPly® 8552 Epoxy Matrix embedded with IM7 carbon fibers obtained from Hexcel® (Ref. 19). For the control panel, no adhesive was placed between the NiTi section and PMC. In the remaining two panels, Hysol® EA9696 (Henkel Corporation) (Ref. 20) or FM® 377U (Cytec Solvay Group) (Ref. 21) thin-film adhesives were used to bond the SMA sheet to the PMC adjacent plies. The precrack insert used in the panels was a thin polyimide film, measuring 0.0127 mm thick, 25.4 mm wide, and 63.5 mm long. The insert was coated with a mold release agent and heated to 200 °C for 1 h in order to prevent the PMC from bonding with the insert.

The composite specimens were assembled into 152.4- by 152.4-mm panels, according to the layup guidelines presented in Figure 1. The panels were processed in an autoclave per the recommended procedure for the HexPly® 8552/IM7 (Ref. 19) PMC panel. The panels were first cured for 1 h at 110 °C under full vacuum and a pressure of 0.1 MPa. The temperature was then ramped up to 176 °C and vacuum vented when the pressure increased beyond 0.2 MPa to a total pressure of 0.68 MPa for 2 h. After curing, each panel was cut into 25.4-mm-wide by 152.4-mm-long specimens for conducting tests. The edges of the specimens were marked using white correction fluid to aid visual detection of crack propagation during testing. The end of the crack insert was marked first, followed by markings placed at 1-mm increments up to 5 mm. Additional markings were placed at 5-mm increments up to 50 mm. Piano hinges were then attached to the precrack end of the specimen using a 3M™ Scotch-Weld™ Structural Adhesive Film AF 163-2M thin-film adhesive (3M™) (Ref. 22). Figure 2 shows an image of a test specimen taken during the testing process.
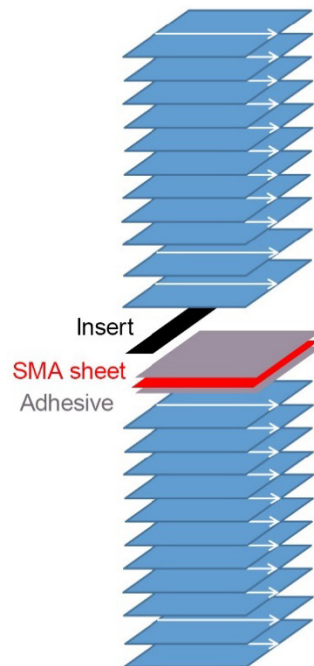

Figure 1.—Panel layup configuration for double cantilever beam testing with 11 plies on each side of shape memory alloy (SMA) sheet bonded with thin-film adhesive, nonstick insert included as precrack.
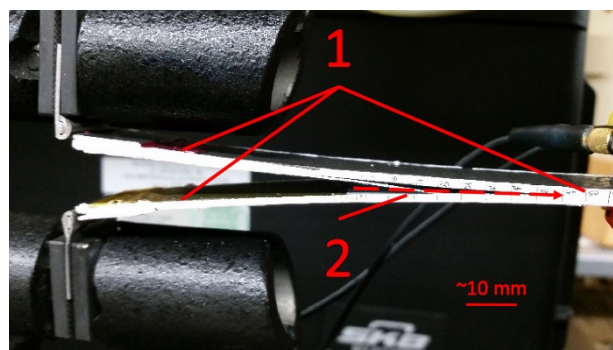

Figure 2.—Double cantilever beam specimen (1) with crack propagation (2) during test. Piano hinge placement was reversed to induce proper break.

2.3   Mechanical Testing

Tests were conducted on an Instron® 5582 testing device (Instron® Corporation) running the Bluehill® V 2.0 software suite (Instron® Corporation). Two acoustic sensors were attached along the center line of the specimen at 12.7 and 25.4 mm from the end of the specimen (opposite the hinges). Vacuum grease was used to maintain contact with the specimen while the clips held the sensors to the specimen. The acoustic sensors were connected to a Digital Wave preamplifier (Digital Wave Corporation), which in turn was connected to a computer running the WaveExplorer software suite (Digital Wave Corporation). The AE sampling rate was 10 MHz, while 2,048 data points for each waveform were recorded, which also included 512 data points per trigger point. Lead break tests were performed on the specimens first to make sure that the AE sensors were placed at the correct locations and functioning properly. A DCB setup was used for testing. The DCB tests involved pulling the sample apart at the bonded hinges, with the crack propagation starting at one end.

The initial crack length (a_o) was measured from the loading hinge of the piano grip to the end of the crack insert. A constant load rate of 5 mm/min was used for the initial loading; once the crack propagated 3 to 5 mm past a_o, the specimen was unloaded back to the starting point at 25 mm/min. The specimen was then loaded again until the crack propagated to the final marks on the specimen (i.e., 50 mm from the end of the crack insert). Once the crack reached the end of the specimen, the test was stopped, and the specimen was unloaded back to the starting point at 25 mm/min.

A Point Grey Research Grasshopper®3 (FLIR® Integrated Imaging Solutions, Inc.) Universal Serial Bus (USB) camera attached to a computer running the FlyCapture software suite (FLIR® Integrated Imaging Solutions, Inc.) was used to take pictures of the crack propagation process every 0.5 s. Figure 3 shows a representative image.

As the specimens were pulled apart, acoustic events were recorded and marked at each point that they occurred. Before the start of each test, pencil lead breaks (0.5 mm diam.) were performed at the edge of the samples so that the sound traveled across both sensors. The time difference of arrival between the sensors was monitored for the first peak (extensional mode). From these peaks, the speed of sound across the specimens was calculated by the distance between the two sensors (x) divided by the difference in arrival time (Δt_x).

Failed specimens were subjected to post-test optical and scanning electron microscopy. Optical microscopy was performed on an Olympus Macroscope DFC295 (Olympus Corporation) utilizing the Leica Applications Suite software (Leica Microsystems), while scanning electron microscopy (SEM) was performed on a Hitachi S–4700 (Hitachi High Technologies in America).
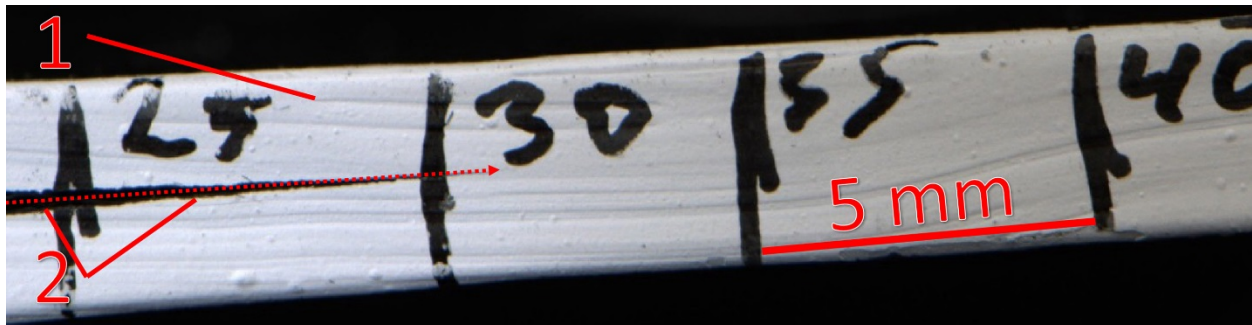

Figure 3.—Side view of double cantilever beam specimen (1) showing crack propagation (2) for specimen 1-4.

3.0 Results

The analysis of data yielded information on fracture toughness. The AE energy signals recorded at the time of the experiments were added to load versus extension graphs to facilitate data interpretation.

3.1 Mechanical Properties

A representative set of load versus displacement data are presented in Figure 4. These graphs are produced from the total data generated from the Bluehill® software during DCB testing. Figure 4(a) represents the DCB load versus displacement data for the control specimens (with no SMA sheet), Figure 4(b) represents the DCB load versus displacement data for the SMA control series, while Figure 4(c) and (d) represent the DCB load versus displacement data for the SMA composites with FM® 377U and Hysol® EA9696 adhesive, respectively.

Each graph in Figure 4 shows the four specimens used for each test group; for example, specimens 1-1, 1-2, 1-3, and 1-4 are the specimens making up the control group (Figure 4(a)). Results from the control group were typical of a composite DCB test; failure was gradual and occurred after a set point of failure began propagation of the crack through the specimen. The addition of the SMA for the SMA control group (Figure 4(b)) led to erratic crack propagation and early failure within the specimens. The addition of FM® 377U adhesive to the SMA in Figure 4(c) helped regulate crack propagation, but still gave low crack growth initiation load. The addition of Hysol® EA9696 adhesive to the SMA in Figure 4(d) not only aided in stable crack propagation during testing, but gave rise to higher loads than were seen in the control group (Figure 4(a)).
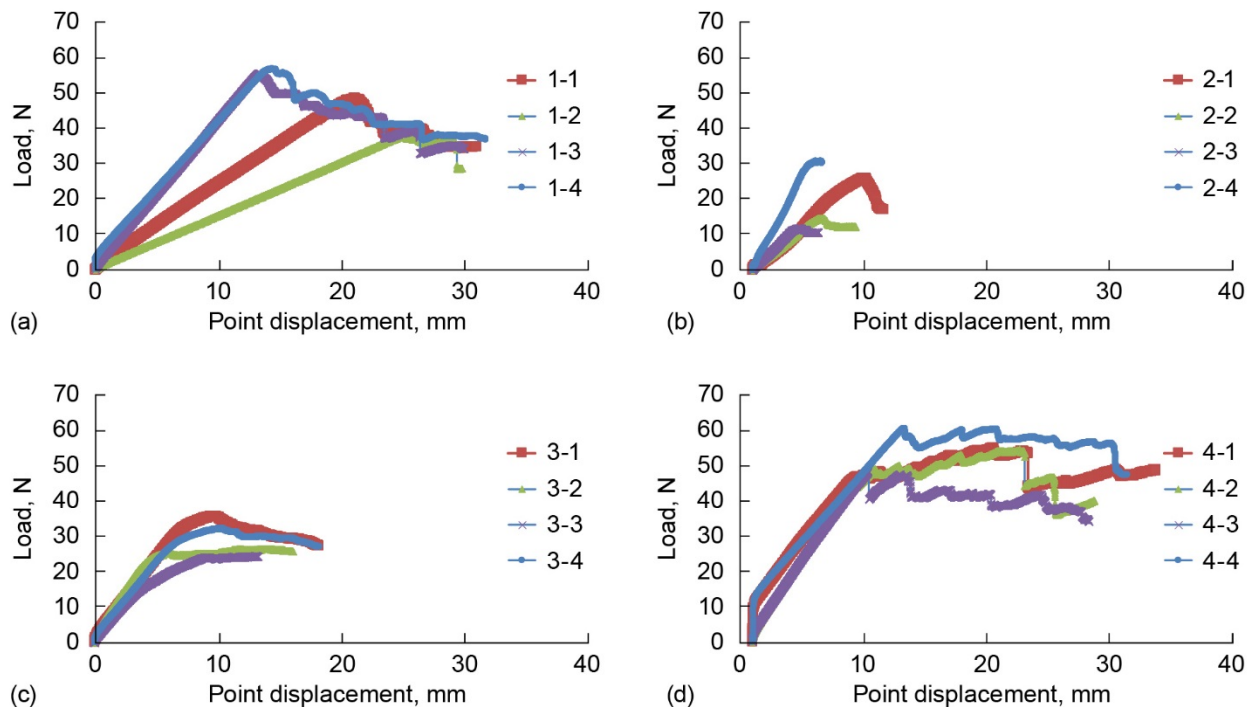

Figure 4.—Load versus displacement graphs. (a) Control. (b) Shape memory alloy (SMA) control. (c) SMA with FM® 377U adhesive. (d) SMA with Hysol® EA9696 adhesive.

3.2   Acoustic Emission (AE) Results

Acoustic signals generated during DCB testing were recorded by the WaveExplorer software via the acoustic sensors and preamplifier. Cumulative AE data are plotted alongside load data versus time for each test specimen to correlate the acoustic signals originating from mechanical events. The majority of acoustic events were detected after crack growth initiation; Figure 5 to Figure 8 present such data.

In these figures, the red lines indicate the load of the specimen during testing, while the blue lines indicate the cumulative AE signal generated during testing. For the control specimens shown in Figure 5, acoustic energy was only generated during the crack propagation phase of the DCB test. This shows that in a control situation there is a direct link between crack propagation within the structure and acoustic energy produced.

Figure 6 shows the irregularity of acoustic data generated when a layer of SMA is introduced within the system without adhesive bonding. Acoustic signals are minimal (with the exception of specimen 2-4), indicating that low-energy crack propagation occurs between the plies of PMC and SMA ply. This is a clear indication of a poor bond between the materials. The introduction of FM® 377U adhesive to the specimen in Figure 7 shows a direct increase in the load during DCB testing, but that failure between the adhesive and PMC material generates low-energy acoustic signals. The same phenomenon is shown in Figure 8, where the addition of Hysol® EA9696 adhesive increases load capabilities during the DCB test but still gives rise to low-energy acoustic signals.
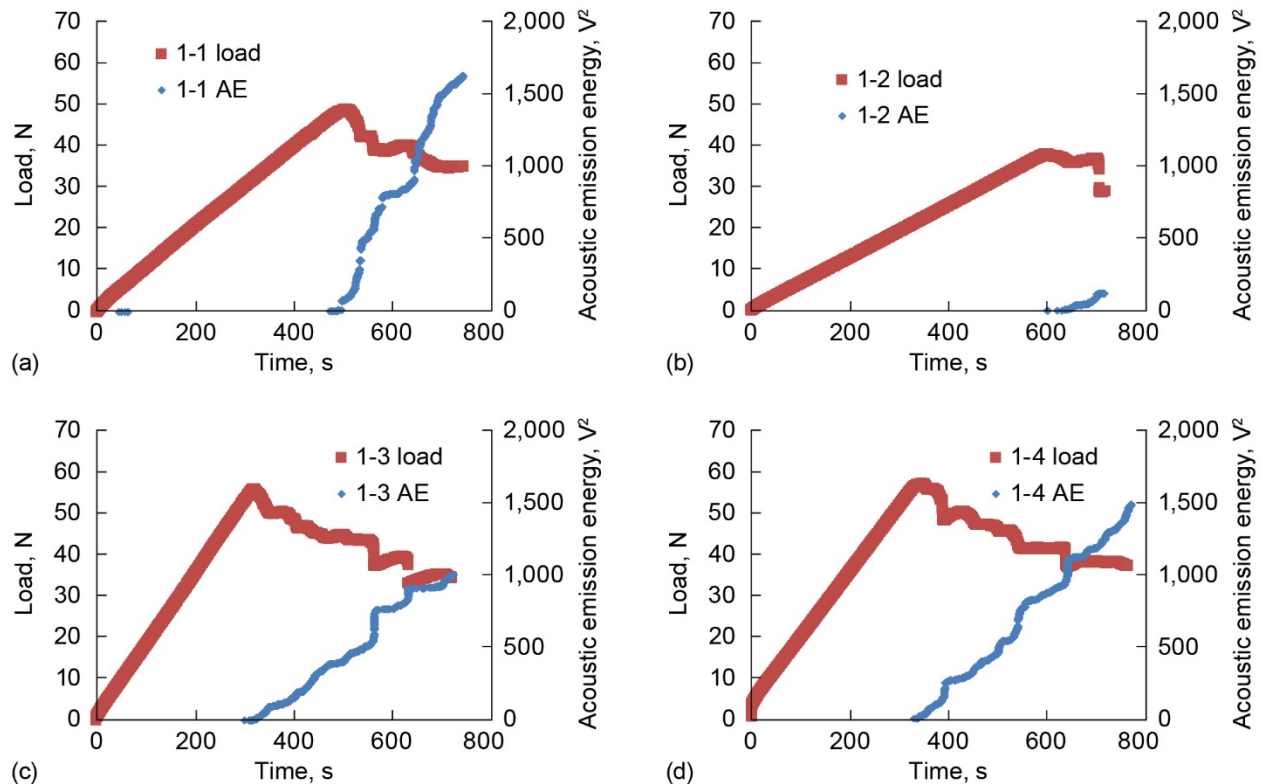

Figure 5.—Load and cumulative acoustic emission (AE) energy versus time for control series. (a) 1-1. (b) 1-2. (c) 1-3. (d) 1-4.
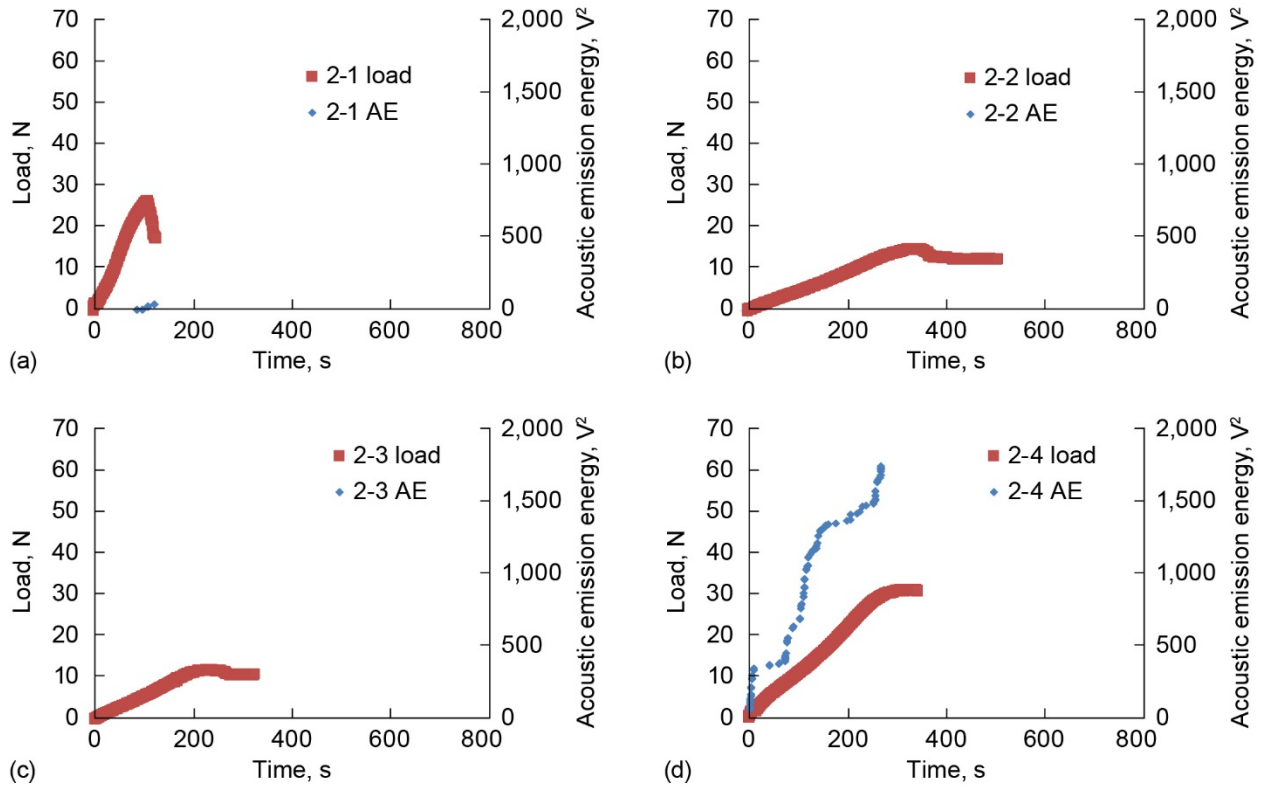
Figure 6.—Load and cumulative acoustic emission (AE) energy versus time for shape memory alloy control series. (a) 2-1. (b) 2-2. (c) 2-3. (d) 2-4.
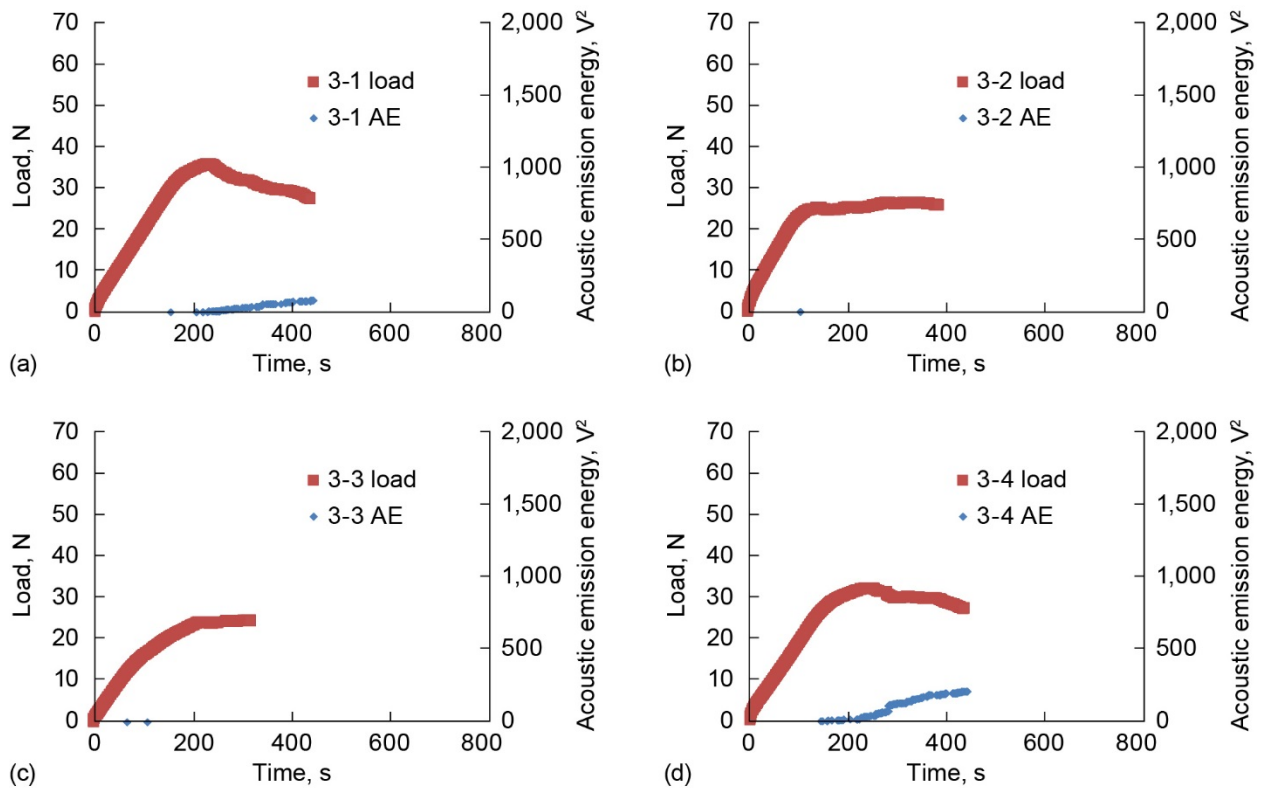

Figure 7.—Load and cumulative acoustic emission (AE) energy versus time for shape memory alloy with FM® 377U adhesive series. (a) 3-1. (b) 3-2. (c) 3-3. (d) 3-4.
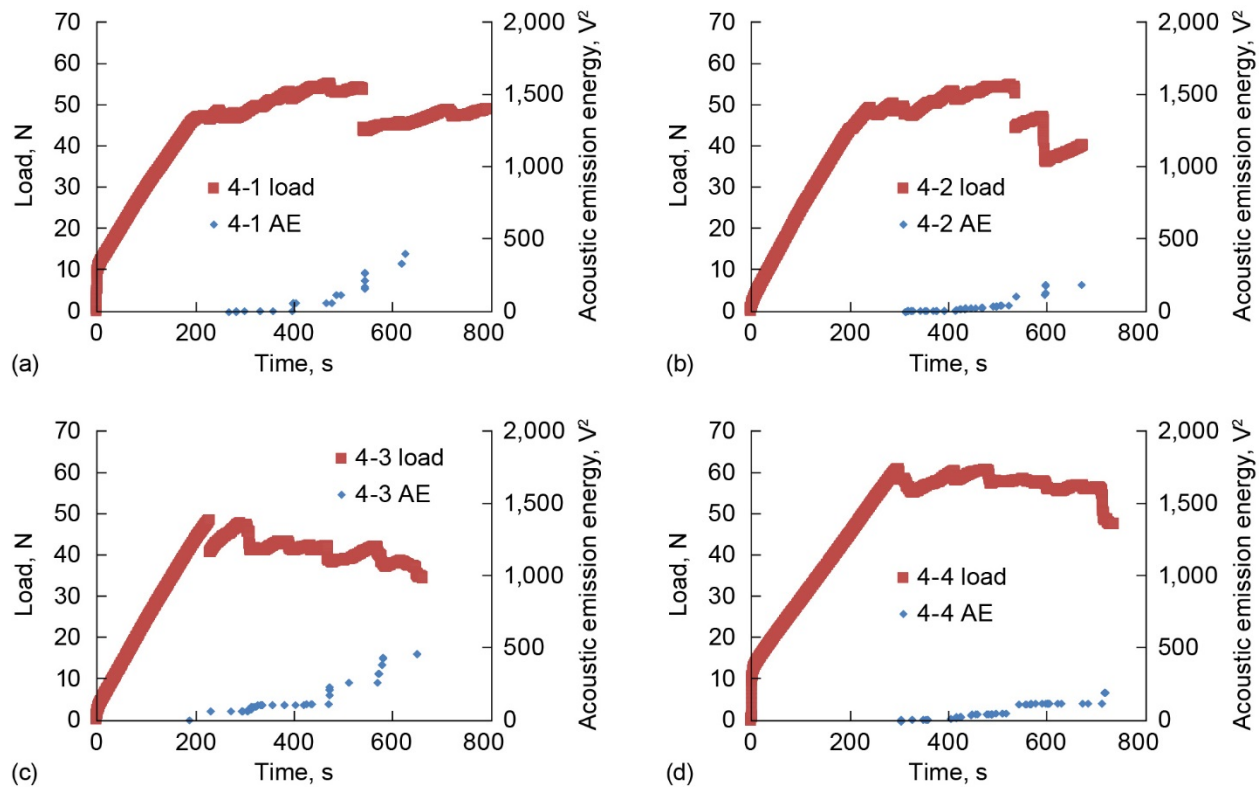
Figure 8.—Load and cumulative acoustic emission (AE) energy versus time for shape memory alloy with Hysol® EA9696 adhesive series. (a) 4-1. (b) 4-2. (c) 4-3. (d) 4-4.

3.3   C-Scan and Microscopy Results

The effects of the SMA inserts and the adhesives on the DCB tests were evaluated by examining the images taken using C-scan, optical microscopy, and SEM methods. The images of the sections of the specimen interiors before and after mechanical tests were compared. These images highlighted the effect of the insert, the nature of the adhesives used, and the issues that caused irregular results in DCB testing.

3.3.1   C-Scan Results

The quality of the manufactured panels was examined by C-scan as a nondestructive method of evaluating a composite by two-dimensional scanning. Figure 9 shows the results. In these images, the dark orange or red colors from the C-scan images are indicative of a well-consolidated segment. The zones with dark or lighter blue color indicate poor bonding, while white sections typically represent the voids or unbonded areas. Figure 9(a) shows the control panel being a well-consolidated area with better overall adhesion. Figure 9(b) shows that a poor bond has developed not only where the SMA has been inserted, but also between the PMC and nonstick insert itself. The addition of FM® 377U adhesive in Figure 9(c) improves this bond, while the addition of Hysol® EA9696 adhesive in Figure 9(d) further degrades this bond.

3.3.2   Photography

Photographs were taken of the parts recovered after mechanical testing and before conducting optical microscopy. DCB specimens were fully separated after testing. The images in Figure 10 are the DCB sections where the SMA was no longer attached.
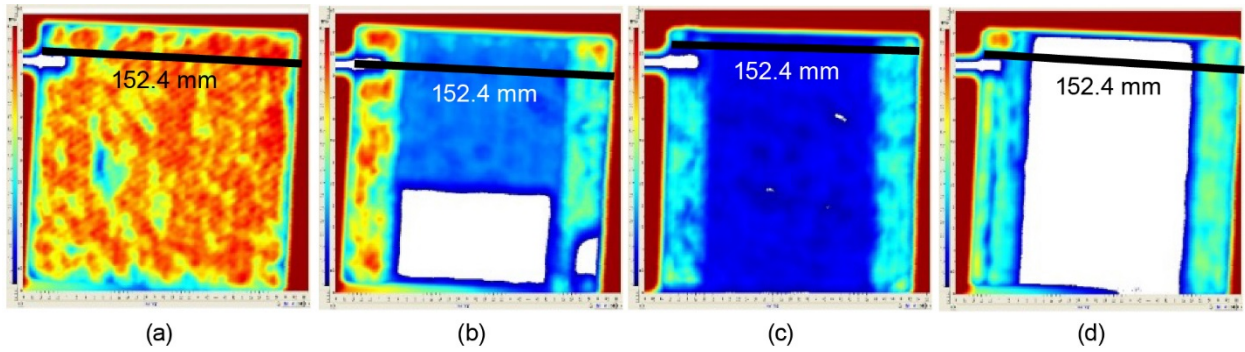
Figure 9.—C-scans of double cantilever beam panels before testing. (a) Control panel. (b) Shape memory alloy (SMA) control panel. (c) SMA with FM® 377U adhesive panel. (d) SMA with Hysol® EA9696 panel.
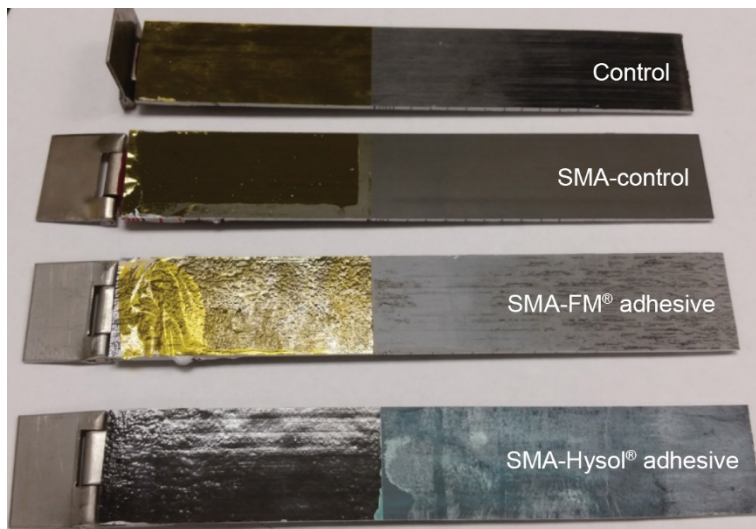

Figure 10.—Post-test images of double cantilever beam specimens. SMA, shape memory alloy.

3.3.3 Optical Microscopy

The optical microscope images of specimens shown in Figure 11 highlight the end of the crack length (a = 50 mm).

Figure 12 shows optical images of SMA specimens 2-1, 3-3, and 4-2, and highlights the bridging effect that occurred between the SMA strip and the PMC plies during DCB testing. This is a ramification of the crack propagation phenomenon seen earlier in Figure 2. The crack traveled from one side of the PMC to the other, while the SMA bridged the gap between the lower and the upper halves of the specimen during DCB testing. This phenomenon was observed for all specimens that had SMA inserts.

3.3.4 Scanning Electron Microscopy (SEM)

SEM images were taken of the area in which the precrack insert was placed, the area in which crack propagation occurred, and (when applicable) the bonded surface of the SMA in the area in which crack propagation occurred. Figure 13 shows the insert area and the crack area of specimen 1-2.

It is observed that the images in Figure 13 portray extensive bubbling in the crack insert area, while the fiber and the matrix breaks are apparent in the crack propagation area images. Figure 14 shows similar images for specimen 2-4, note that in this case the specimen contained SMA but no adhesive.

For specimen 2-4, the crack insert area was fairly smooth with no noticeable bubbles, while the crack propagation area showed little sign of fiber breaks. The texture of the specimen image is formed from processing alongside the SMA. Figure 15 shows SEM images of the PMC crack insert and crack propagation areas for specimen 3-1, which contained FM® 377U adhesive to aid bonding of the SMA strip with the PMC plies. This figure also shows the SMA surface in the crack propagation area.
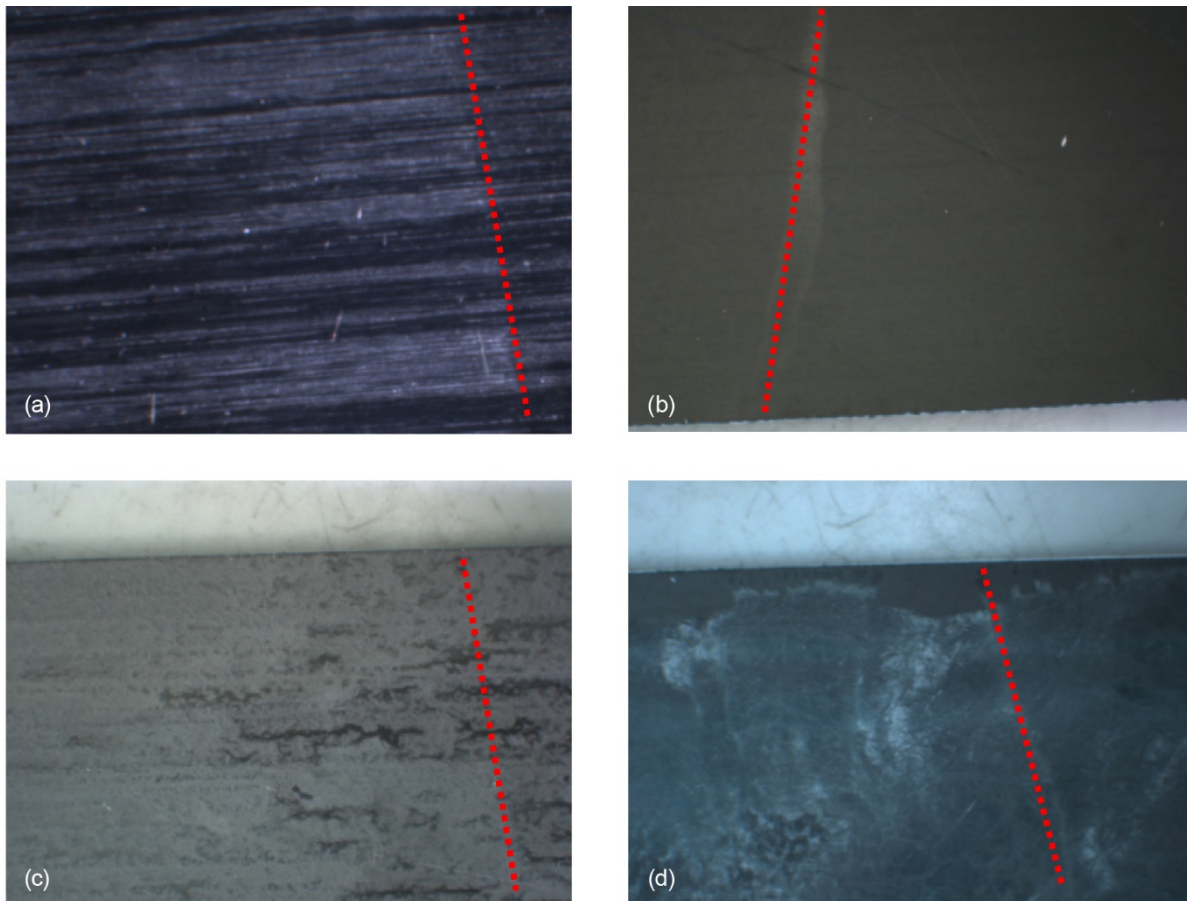

Figure 11.—Crack propagation ends of double cantilever beam specimens. (a) Control. (b) Shape memory alloy (SMA) control. (c) SMA with FM® 377U adhesive. (d) SMA with Hysol® EA9696 adhesive.
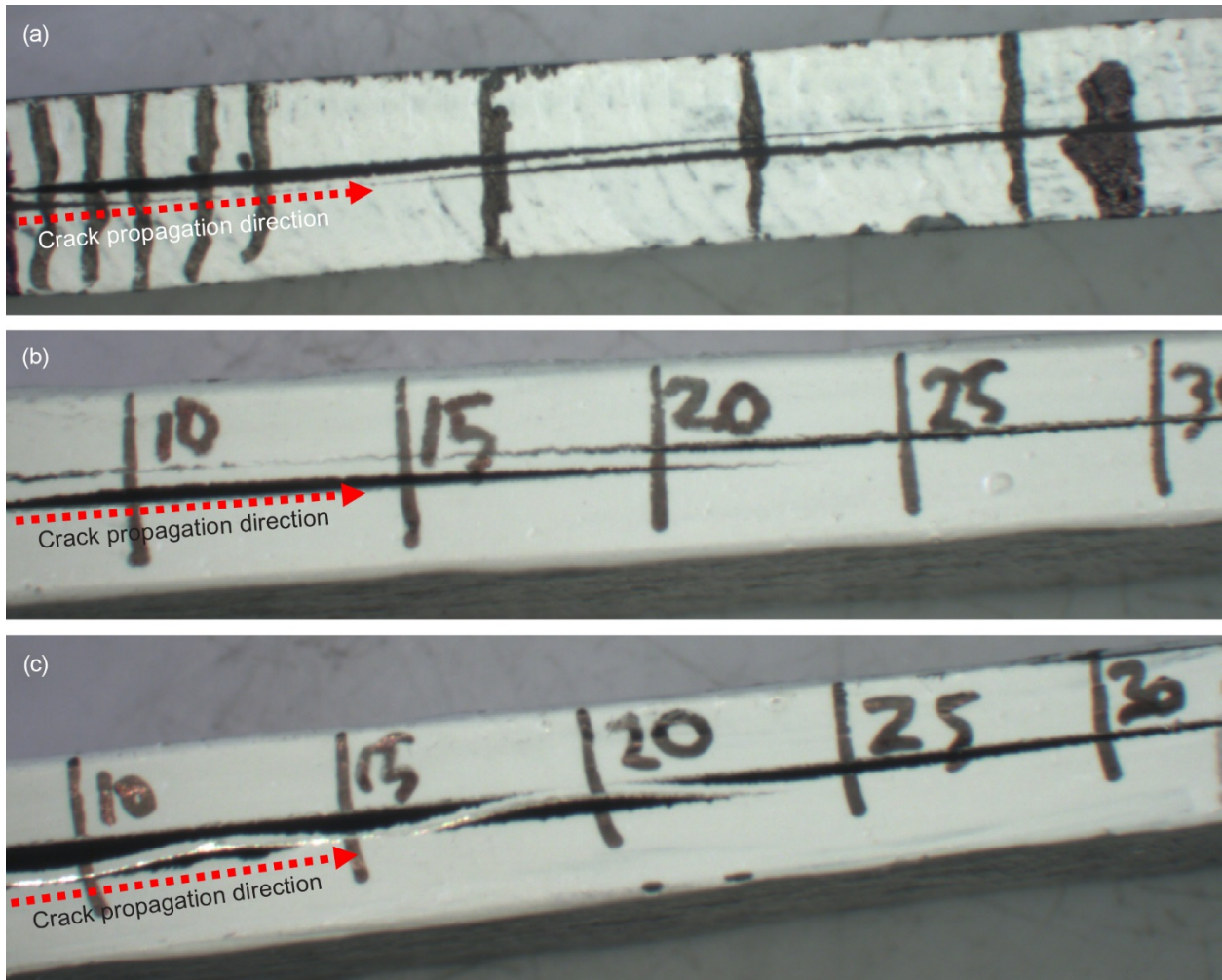
Figure 12.—Shape memory alloy bridging. (a) Specimen 2-1. (b) Specimen 3-3. (c) Specimen 4-2.
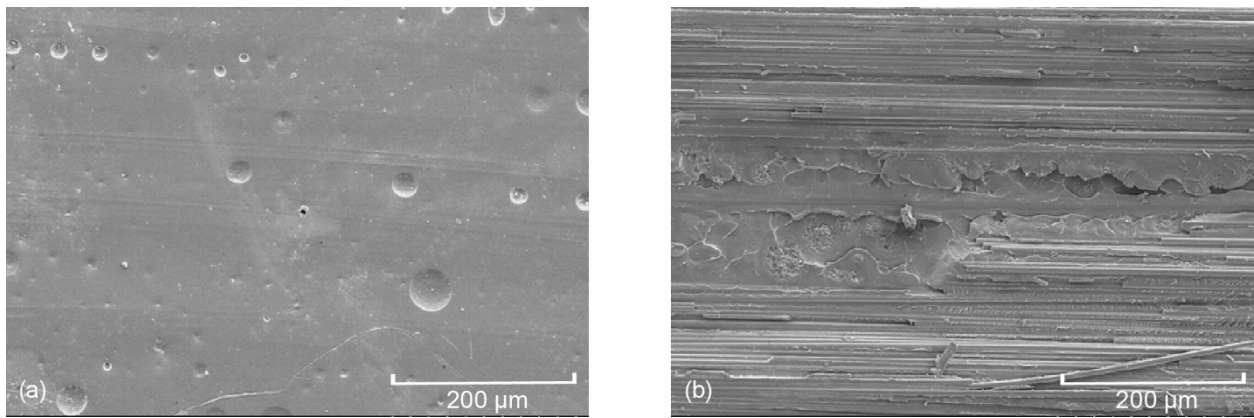

Figure 13.—Scanning electron microscopy images of specimen 1-2. (a) Crack insert area. (b) Crack propagation area.
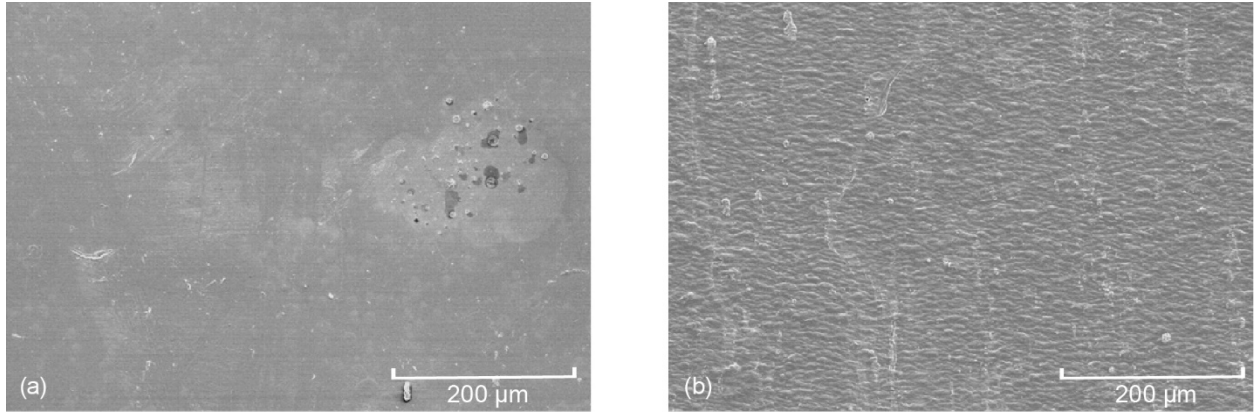
Figure 14.—Scanning electron microscopy images of specimen 2-4. (a) Crack insert area. (b) Crack propagation area.
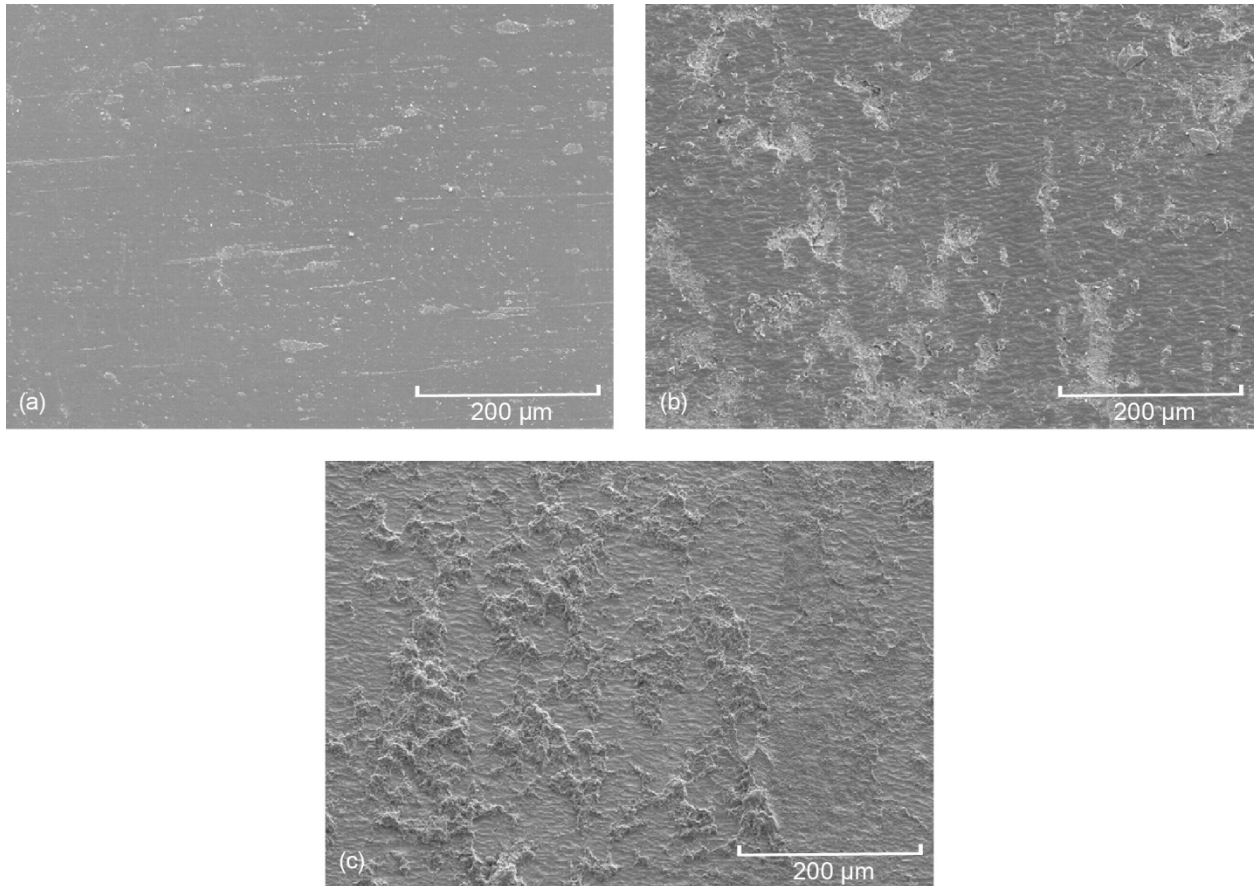

Figure 15.—Scanning electron microscopy images of specimen 3-1. (a) Polymer matrix composite (PMC) crack insert area. (b) PMC crack propagation area. (c) Shape memory alloy crack propagation area.
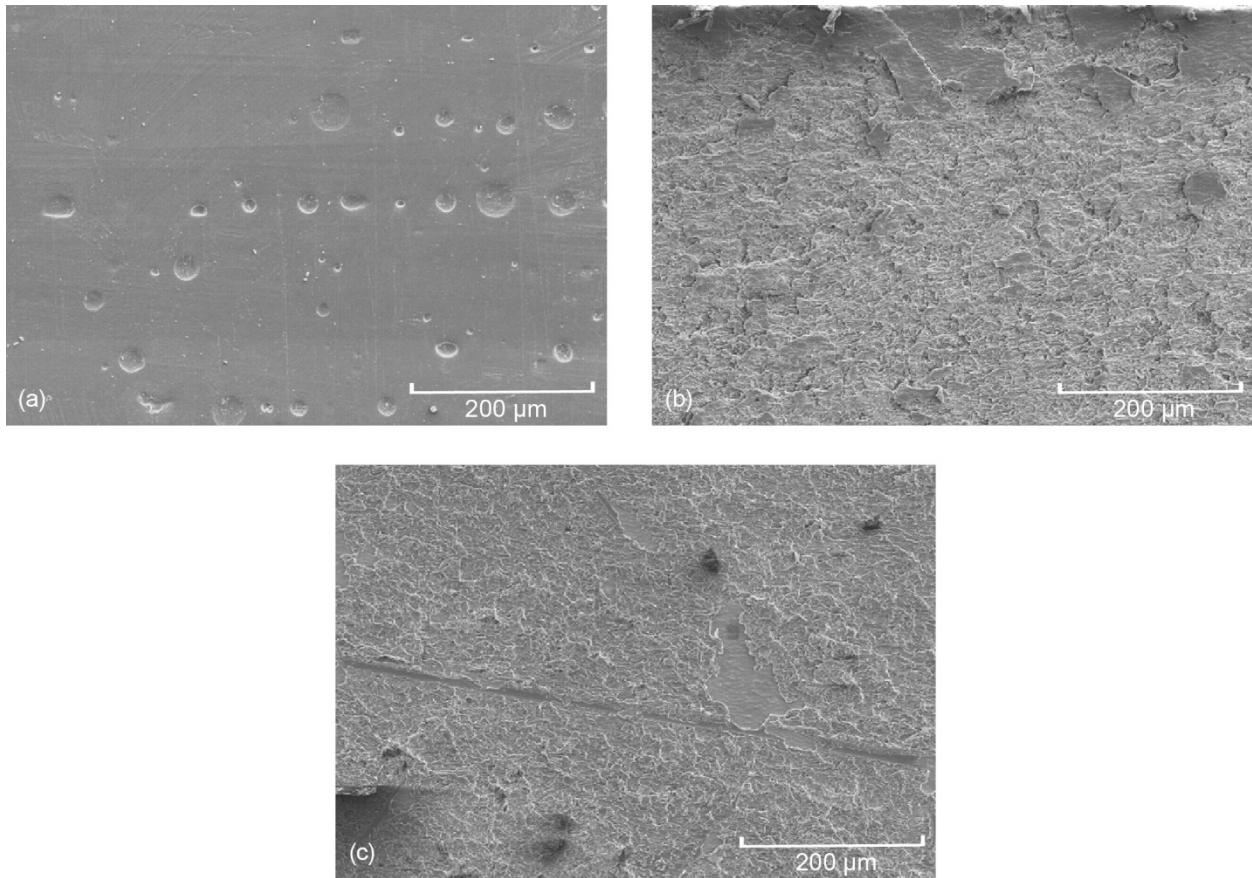
Figure 16.—Scanning electron microscopy images of specimen 4-1. (a) Polymer matrix composite (PMC) crack insert area. (b) PMC crack propagation area. (c) Shape memory alloy crack propagation area.

The images in Figure 15 indicate that the FM® 377U adhesive preferentially bonded with the PMC as is apparent from the large amounts of FM® 377U residue on the PMC side of the specimen. The images of the SMA show only small amounts of the FM® 377U residue. Figure 16 shows SEM images of the PMC crack insert and the crack propagation areas of specimen 4-1. In this case, Hysol® EA9696 adhesive was used to aid in the bonding between the SMA and PMC.

A comparison of the images presented in Figure 16 with those of Figure 15 shows that the Hysol® EA9696 adhesive remnants are almost evenly distributed between the SMA strip and the PMC panel. The image in Figure 16(a) indicates the presence of bubbles on the PMC crack insert area similar to those seen in Figure 13.

4.0 Analysis

A numerical analysis of the results from DCB testing was performed in order to highlight the differences in interlaminar toughness between the sets of specimens. This analysis utilizes the three recommended methods of calculating the Mode I interlaminar toughness (G_{IC}) of the tested specimens, namely, modified beam theory (MBT), compliance calibration (CC), and modified compliance calibration (MCC).

4.1 Modified Beam Theory (MBT)

The DCB test data were first analyzed by correlating the delamination length with the displacement. The results are summarized in Figure 17. This figure shows via graph and imagery the correlation between load and point displacement and delamination length. The red stars on the blue load line indicate when certain delamination lengths have been reached (with corresponding pictures of the delamination length).

The beam theory expression for the strain energy release rate of a perfectly built-in DCB is given in Equation (1) (Ref. 18):

$$G_I = \frac{3P\delta}{2ba} \tag{1}$$

where G_I is the strain energy release rate, P is the load, δ is the load point displacement, b is the specimen width, and a is the delamination length.

This equation overestimates the value of G_I due to possible rotation that may occur at the delamination front (Ref. 18). One method used to correct for this rotation is to treat the DCB test as if there were a slightly longer delamination, $a + |\Delta|$, where Δ is calculated experimentally by the generation of a least squares plot of the cube root of compliance ($C^{1/3}$) as a function of the delamination length (Ref. 18). Compliance (C) is the ratio of the load point displacement to the applied load (δ/P). This is the essence of the MBT, which is used to calculate the Mode I interlaminar fracture toughness via Equation (2):
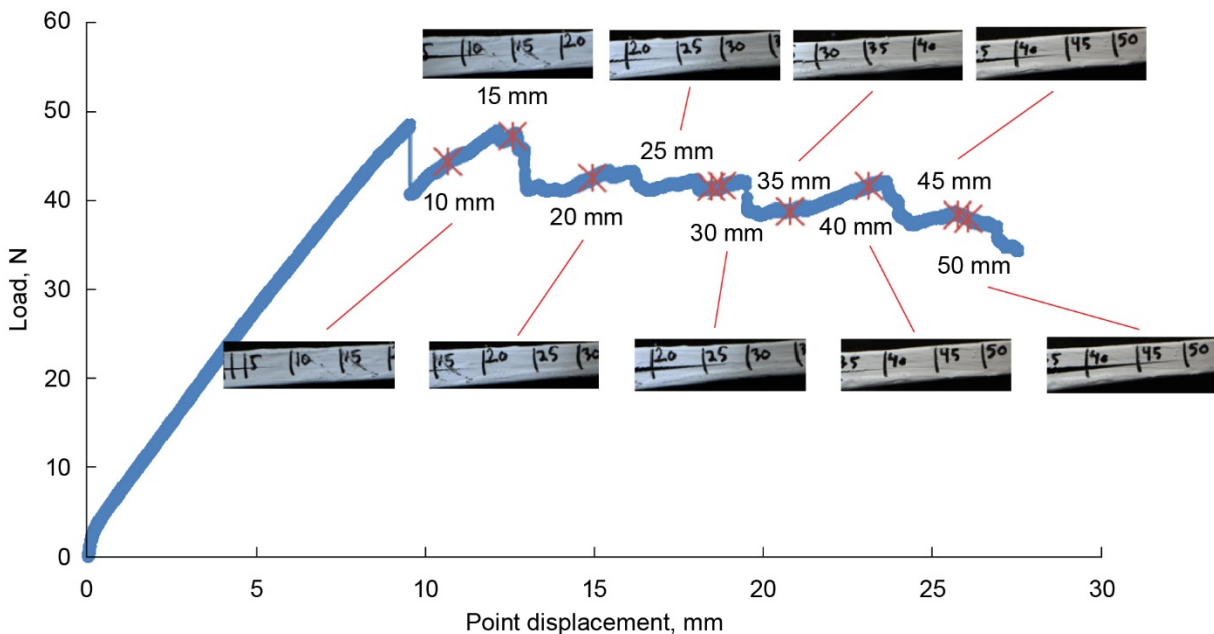
$$G_{IC} = \frac{3P\delta}{2b(a + |\Delta|)} \tag{2}$$

Figure 17.—Correlation between crack length and separation displacement during double cantilever beam testing for specimen 4-3.
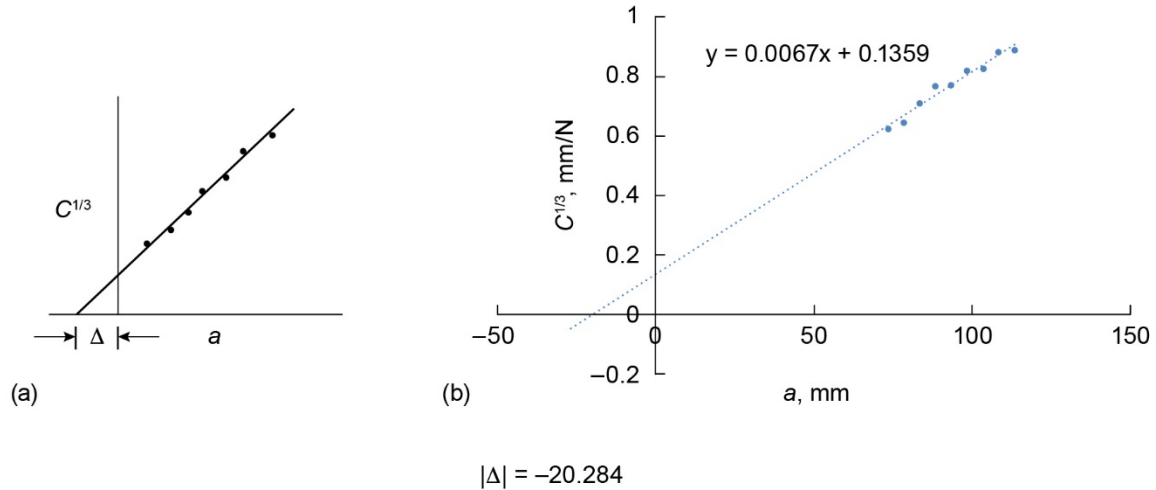
$$|\Delta| = -20.284$$

Figure 18.—Modified beam theory for C, compliance; a, delamination length; and Δ, least square root plot offset value. (a) Schematic. (b) Actual graphical application.

In Equation (2), Δ is the least square root plot offset value. Figure 18(a) shows schematically how the value of Δ is calculated, while Figure 18(b) shows the actual calculation from experimental data for specimen 4-3.

4.2   Compliance Calibration (CC)

The CC method (Ref. 18) generates a least squares plot of log (δ_i/P_i) against the log (a_i) values from the visually observed delamination onset and the propagation. By fitting a least squares line to the plotted data, the exponent n (slope of the line) can be determined. This value of n is then utilized in Equation (3) to obtain the values of G_{IC}:

$$G_{IC} = \frac{nP\delta}{2ba} \tag{3}$$

In Equation (3), n is the slope. Figure 19(a) shows schematically how the n value can be obtained from a data fit, while Figure 19(b) shows the least square fit of the experimental data for specimen 4-3 to obtain the value of $n = 2.5062$.

4.3   Modified Compliance Calibration (MCC)

The MCC method (Ref. 18) utilizes a least squares plot of the delamination length normalized by the specimen thickness (a/h) against the cube root of compliance ($C^{1/3}$). This data is generated from the visually observed delamination onset values along with propagation values. From this line, a slope (A_1) is found and is used in determining the value of G_{IC} as in Equation (4):

$$G_{IC} = \frac{3P^2C^{2/3}}{2A_1bh} \tag{4}$$

In Equation (4), C is the compliance (δ/P), A_1 is the MCC value, and h is the specimen thickness.

Figure 20 shows a schematic of the calculation of the A_1 value (Figure 20(a)), along with the application for specimen 4-3 (Figure 20(b)).

$n = \Delta_y/\Delta_x$

$y = 2.5062x - 5.2847$

$n = 2.5062$
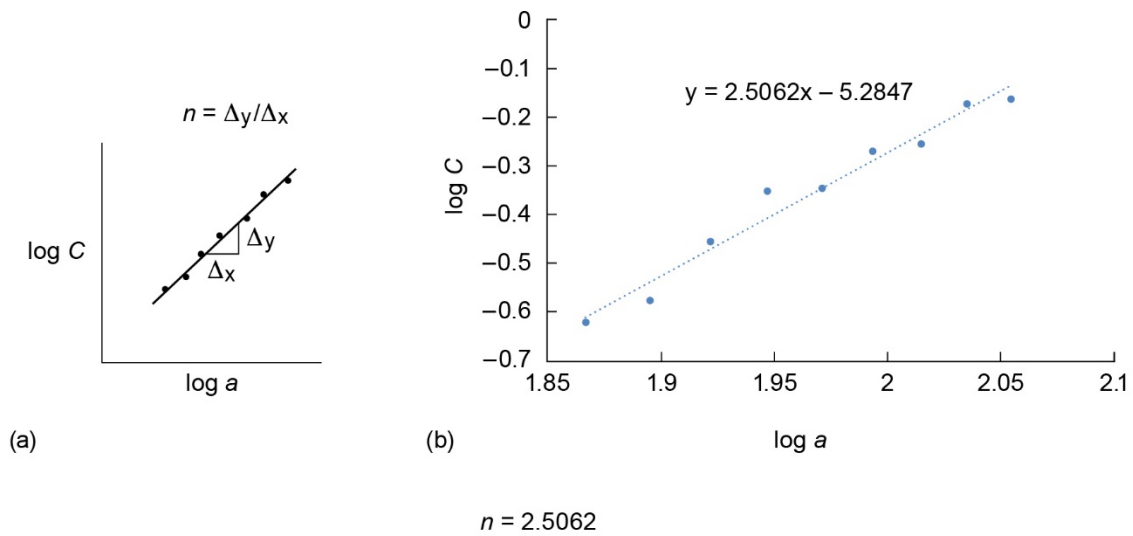
Figure 19.—Compliance calibration of C, compliance; a, delamination length; and n, slope of line. (a) Schematic. (b) Actual graphical application.

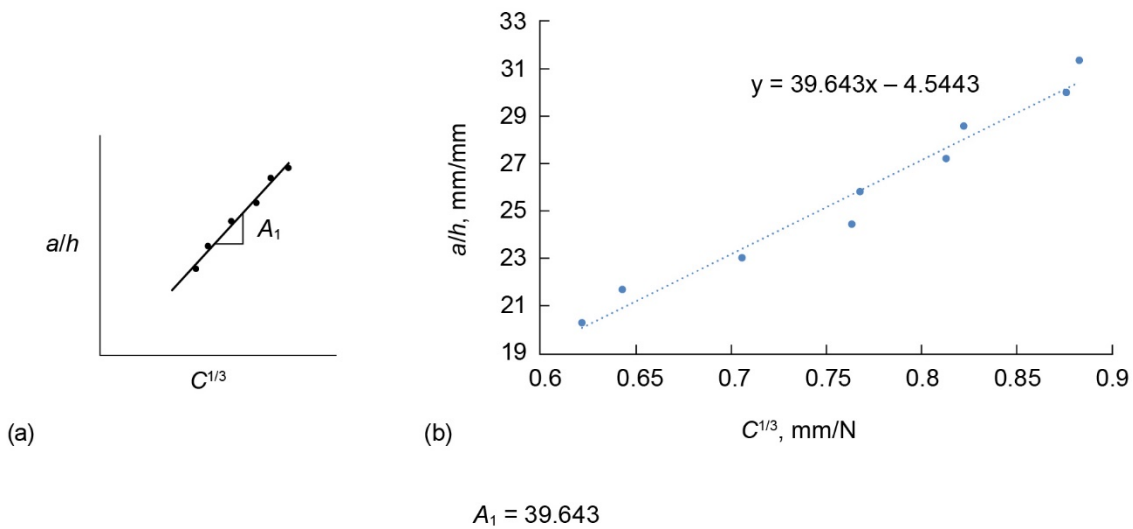$y = 39.643x - 4.5443$

$A_1 = 39.643$

Figure 20.—Modified compliance calibration (MCC) A_1, MCC value; a, delamination length; C, compliance; and h, specimen thickness. (a) Schematic. (b) Actual graphical application.

4.4 Mode I Interlaminar Toughness (G_{IC}) Values

The G_{IC} values calculated from the use of three methods described above were plotted against the delamination length in order to obtain the delamination resistance curves of the specimens. Unfortunately, the delamination length propagation of the SMA-control specimen (Series 2) was so chaotic that calculation of reasonable G_{IC} values for this set of specimens was not possible. The crack propagation speed was sporadic in nature, and the crack progressed at significantly different rates on either side of the test specimen during delamination.

Figure 21 to Figure 23 show delamination resistance curves (or *R* curves) for various specimen sets. The blue data points represent the MBT method, the red data points represent the CC method, and the green data points represent the MCC method.

The *R* curves shown in Figure 21 are typical of a PMC composite system (Ref. 23). The line based on the MBT equation in blue is typically three to four times higher than the CC methods (Ref. 18). Both the CC and MCC methods are typically in agreement with each other. These results are minimized in Figure 22, where an SMA insert is bonded to the PMC via the FM® 377U adhesive. The low G_{IC} values in the *R* curves in Figure 23 indicate that the addition of the FM® 377U adhesive was very poor in terms of increasing the strain energy release rate of the system. The addition of Hysol® EA9696 adhesive, however, had the opposite, positive effect. Figure 23 shows that the addition of Hysol® EA9696 adhesive between the SMA and PMC layers increases the strain energy release rate to levels beyond those shown in the control specimen of Figure 21.
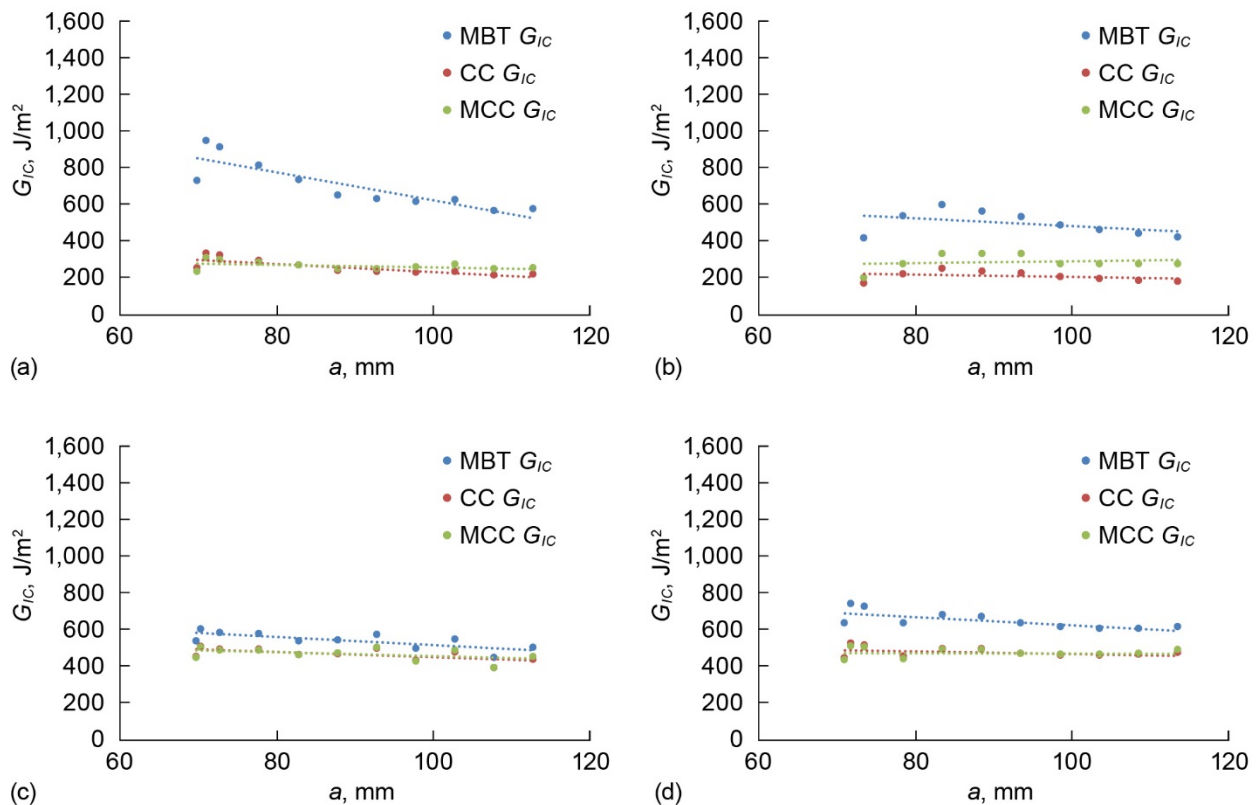
Figure 21.—Delamination resistance curves (*R* curves) for control series. (a) 1-1. (b) 1-2. (c) 1-3. (d) 1-4. G_{IC}, Mode I interlaminar toughness; *a*, delamination length; CC, compliance calibration; MBT, modified beam theory; MCC, modified compliance calibration.

Figure 22.—Delamination resistance curves (*R* curves) for shape memory alloy with FM® 377U adhesive series. (a) 3-1. (b) 3-2. (c) 3-3. (d) 3-4. G_{IC}, Mode I interlaminar toughness; *a*, delamination length; MBT, modified beam theory; CC, compliance calibration; MCC, modified compliance calibration.

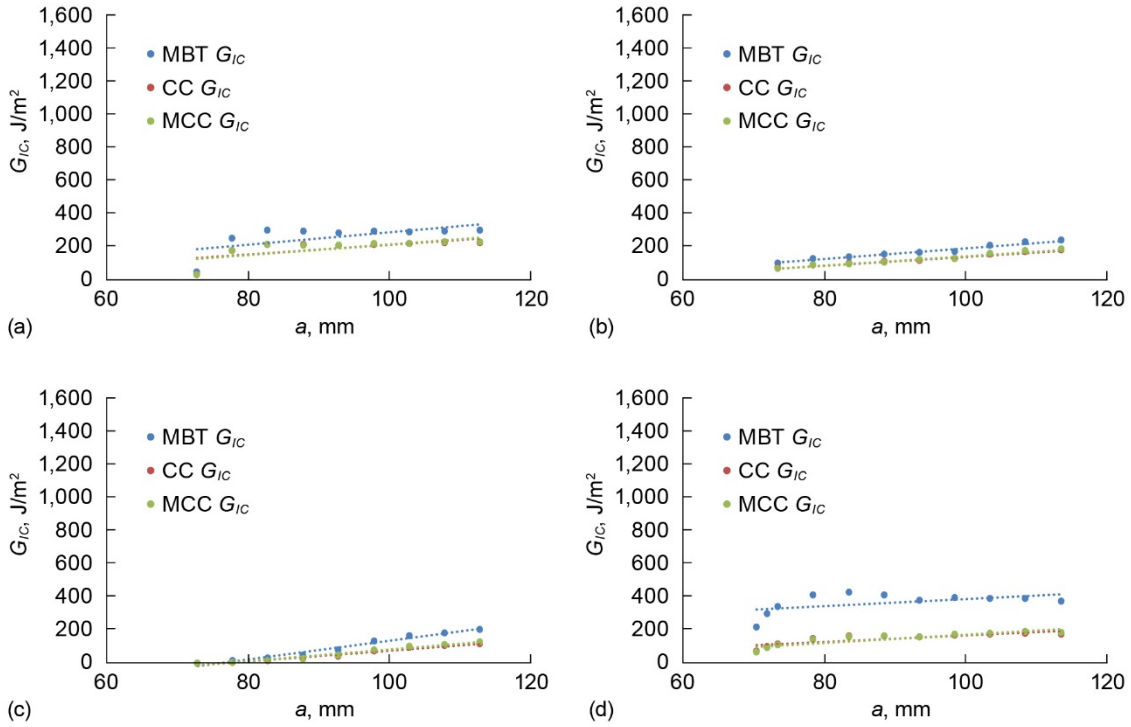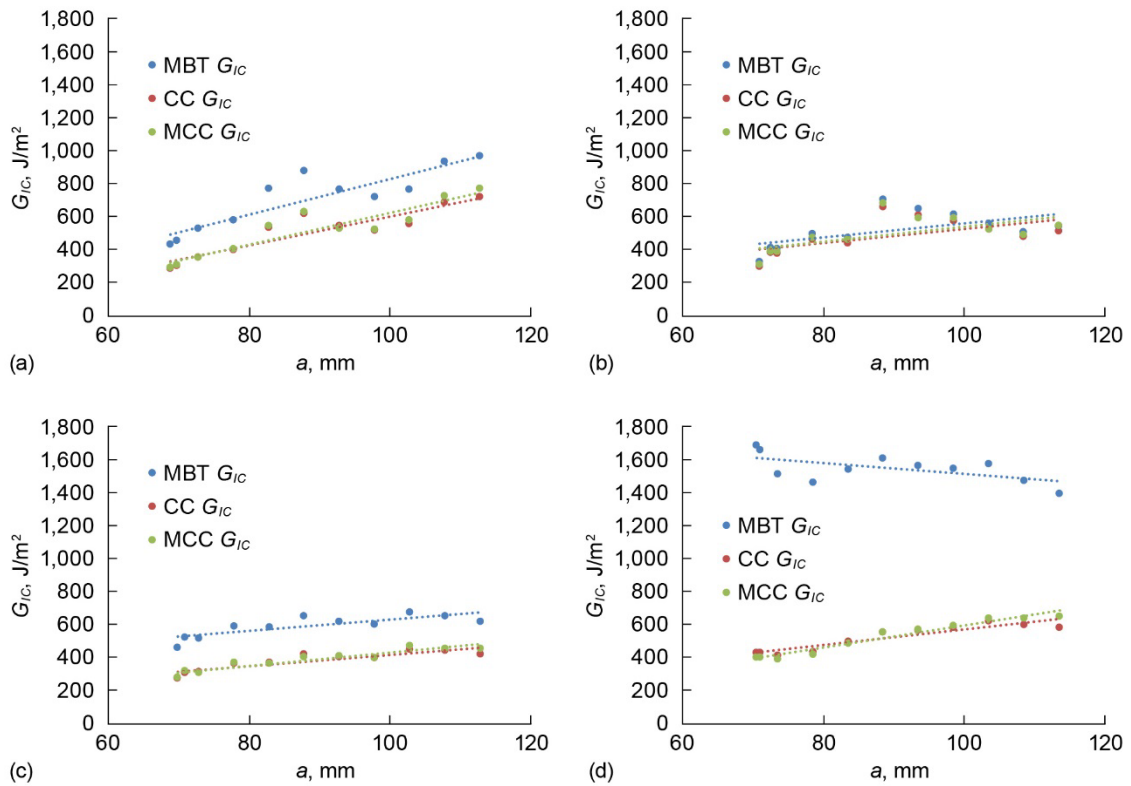Figure 23.—Delamination resistance curves (*R* curves) for shape memory alloy with Hysol® EA9696 adhesive series. (a) 4-1. (b) 4-2. (c) 4-3. (d) 4-4. G_{IC}, Mode I interlaminar toughness; *a*, delamination length; MBT, modified beam theory; CC, compliance calibration; MCC, modified compliance calibration.

5.0 Discussion

The data generated in this study yielded somewhat higher numerical values compared to the data obtained using similar materials in prior work (Refs. 24 to 27). Prior studies reported G_{IC} values of the HexPly® 8552/IM7 specimens around 0.2 to 0.25 KJ/m^2; the results obtained in this study fell in the range of 0.2 to 1.2 KJ/m^2. In addition to higher G_{IC} values, sample sets 1 and 4 also displayed more nonlinear behavior within the *R* curves. In comparison, typical results from DCB testing indicate a quick growth in G_{IC} values after initiation, followed by a constant value (Ref. 28). The discrepancy between the reported results as compared to prior studies is the outcome of both extensive fiber bridging and SMA bridging (discussed below) that occurred during the testing.

5.1 Bridging Effect

Fiber bridging in DCB testing is a well-known phenomenon that has been shown experimentally and numerically to give G_{IC} values higher than what is otherwise expected for a specimen (Refs. 18 and 29 to 33). This is due to fibers bridging the gap between the upper and lower halves of two 0° plies within a DCB specimen during the test.

In typical composite systems, the use of dissimilar ply orientations suppresses fiber bridging during a delamination failure. It is for this reason that research in this area has been aimed at minimizing or eliminating this effect during the DCB test (Refs. 29 to 33). An increase of the toughness values can be attributed to the forces required to break either the bridging fiber between plies or the fiber-matrix bonds between plies (i.e., fiber pullout). The aftermath of fiber bridging can be seen in microscopy images of the crack propagation areas. Figure 24 gives a closeup of fiber breaks that occurred due to bridging.

Fiber bridging is indicated not only by the broken fibers, but also by the fact that the broken fibers have been debonded from the epoxy matrix within the PMC. Fiber bridging was not present in the samples with SMA; the physical barrier provided by the inclusion of the SMA eliminated this bridging effect. The inclusion of the SMA, however, led to another type of bridging effect. This SMA bridging effect was observed during testing of the specimens and has been shown previously in Figure 12. In these images, the crack that propagates between the PMC and SMA, initiated by the polyimide crack insert, switches from one side of the SMA to the other. This phenomenon creates an SMA bridge between the upper and the lower PMC sections of the DCB specimen during the delamination process.
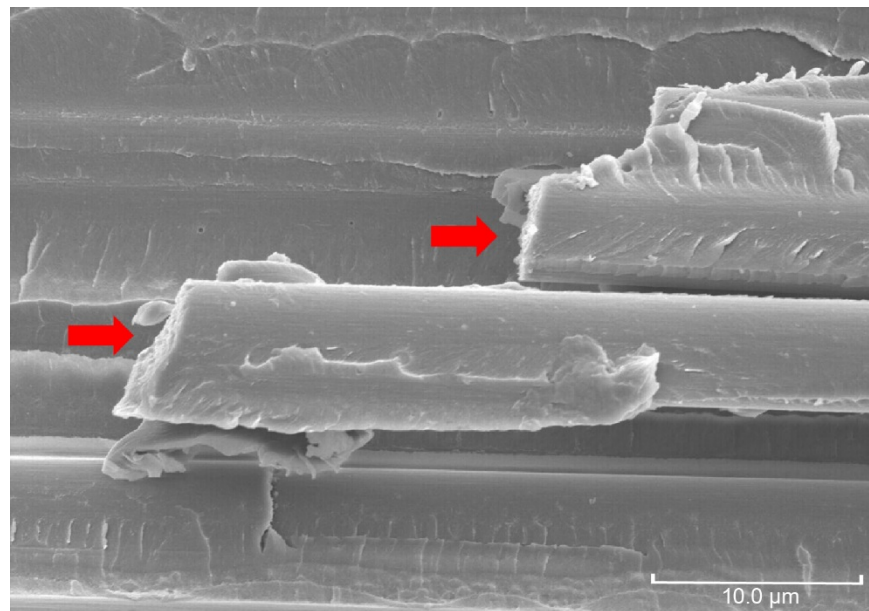

Figure 24.—Fiber breaks due to bridging in specimen 1-2.

Similar to fiber bridging in the control specimen, the SMA bridging contributes to higher loads and higher calculated G_{IC} values. This is reflected in the results shown in Figure 23. The interlaminar toughness was much higher for the specimens containing Hysol® EA9696 adhesive in comparison to the specimens that contained FM® 377U adhesives. This was reflected in the SEM images presented in Figure 15 and Figure 16. In Figure 15, the majority of the remnant FM® 377U adhesive was seen bonded onto the PMC panel, while in Figure 16, a somewhat even distribution of the Hysol® EA9696 adhesive between the PMC and SMA was observed. A stronger bond between the SMA and PMC via Hysol® EA9696 adhesive would also exacerbate the effect of SMA bridging during DCB testing, thus resulting in higher interlaminar fracture toughness values. The only data that does not correlate with better bonding for Hysol® EA9696 than FM® 377U adhesive was C-scan data; the images in Figure 9 show a qualitatively better bond within the panels joined by the FM® 377U adhesive. The inclusion of metal into the panels may negate the usefulness of the C-scan data as a reliable method for monitoring the bond strength.

5.2   Acoustic Emissions (AEs)

The results from the AE monitoring reflected the patterns that were seen in SEM images. For example, the majority of AE energy recorded from samples came from the set of control specimens, shown in Figure 5. These specimens exhibited extensive fiber bridging during testing and thus would be expected to have higher emissive energies.

It has been shown in prior research that different AE energies are seen in composites when different failure mechanisms occur (Refs. 34 to 37). These can include matrix cracks, fiber breaks, and fiber-matrix debonding. These studies, while arriving at differing conclusions on the interpretation of AE results, concluded that the loudest AE events would occur from fiber breaks. This is due to the large amount of energy typically dissipated during this event related to the high stiffness and strength of the carbon fiber. In Figure 7 to Figure 9, the AE events were either nonexistent or minimal compared to the control specimens; this is likely because these AEs were generated from low-energy events such as matrix cracking, fiber-matrix debonding, or adhesive failure during delamination.

The bond strength difference between the two adhesives is reflected in the AE; a stronger bond (verified via SEM) between SMA and PMC was provided by the Hysol® EA9696 adhesive. This bonding resulted in more AE events during delamination as compared to the FM® 377U adhesive bonding.

6.0   Conclusion

This study examined the interaction between a shape memory alloy (SMA) sheet and polymer matrix composite (PMC) plies when subjected to double cantilever beam (DCB) testing. Four different test panels were fabricated and specimens were cut and subjected to testing via the ASTM D5528 test method. During testing, specimens were monitored with acoustic sensors; these acoustic emission (AE) signals were then plotted against loads generated during testing. The Mode I interlaminar toughness (G_{IC}) results were calculated according to the three methods listed by the ASTM test method: modified beam theory (MBT), compliance calibration (CC), and modified compliance calibration (MCC).

Without any preparation of the SMA surfaces, the addition of adhesives to the bond layer between the PMC and SMA was shown to provide stable interlaminar fracture toughness results. Calculated G_{IC} values were higher than previously reported data. This inflation of interlaminar toughness values was attributed to extensive fiber bridging within control samples, along with a newly observed phenomenon of SMA bridging between the SMA and PMC. In these samples, the crack traversed the SMA layer due to discrepancies in bonding between the SMA and PMC as the test progressed. Like fiber bridging, this SMA bridging resulted in extremely high values of interlaminar fracture toughness. Higher toughness values in the Hysol® EA9696 adhesive specimens were due to better bonding between the SMA and PMC. Evidence of this improved bonding was seen directly in post-test scanning electron microscopy (SEM) imaging as well as being reflected in the calculated G_{IC} values and AE levels generated during testing.

Appendix A.—Nomenclature and Symbols

Nomenclature

AE	acoustic emission
CC	compliance calibration
CFRP	carbon fiber reinforced polymer
DCB	double cantilever beam
MAE	modal acoustic emission
MBT	modified beam theory
MCC	modified compliance calibration
PMC	polymer matrix composite
SEM	scanning electron microscopy
SMA	shape memory alloy
USB	Universal Serial Bus

Symbols

a	delamination length
a_o	initial crack length
A_1	slope of (a/h) versus $C^{1/3}$
b	specimen width
C	compliance
G_I	strain energy release rate
G_{IC}	Mode I interlaminar toughness
h	specimen thickness
n	slope of line
P	load
R	resistance
x	distance between two acoustic sensors
Δ	least square root offset value
Δt_x	difference in arrival time
δ	load point displacement

Subscripts

i	ith iteration (for general number order)

References

1. de Araujo, C.J., et al.: Fabrication and Static Characterization of Carbon-Fiber-Reinforced Polymers With Embedded NiTi Shape Memory Wire Actuators. Smart Mater. Struct., vol. 17, 2008, p. 065004.

2. Bollas, D., et al.: Stress Generation by Shape Memory Alloy Wires Embedded in Polymer Composites. Acta Mater., vol. 55, no. 16, 2007, pp. 5489–5499.

3. Parthenios, J.; Psarras, G.C.; and Galiotis, C.: Adaptive Composites Incorporating Shape Memory Alloy Wires. Part 2: Development of Internal Recovery Stresses as a Function of Activation Temperature. Composites Part A, vol. 32, no. 12, 2001, pp. 1735–1747.

4. Schrooten, Jan, et al.: Progress on Composites With Embedded Shape Memory Alloy Wires. Mater. Trans., vol. 43, no. 5, 2002, pp. 961–973.

5. Turner, Travis L., et al.: Fabrication and Characterization of SMA Hybrid Composites. Presented at the SPIE 8th Annual International Symposium on Smart Structures and Materials; Active Materials; Behavior and Mechanics, SPIE Paper 4333–60, 2001, pp. 343, 33–43.

6. Tobushi, Hisaaki, et al.: Thermomechanical Properties of Shape-Memory Alloy and Polymer and Their Composites. Mechanics of Advanced Materials and Structures, vol. 16, no. 3, 2009, pp. 236–247.

7. Turner, Travis L., et al.: Modeling, Fabrication, and Testing of a SMA Hybrid Composite Jet Engine Chevron Concept. J. Intell. Material Syst. Struct., vol. 17, 2006, pp. 483–497.

8. Kim, Cheol; Park, Bum-Sik; and Goo, Nam-Seo: Shape Changes by Coupled Bending and Twisting of Shape-Memory-Alloy-Embedded Composite Beams. Smart Mater. Struct., vol. 11, no. 4, 2002, pp. 519–526.

9. Ostachowicz, W., et al.: Dynamics and Buckling of a Multilayer Composite Plate With Embedded SMA Wires. Compos. Struct., vol. 48, nos. 1–3, 2000, pp. 163–167.

10. Poon, Chi-kin, et al.: Interfacial Debond of Shape Memory Alloy Composites. Smart Mater. Struct., vol. 14, no. 4, 2005, pp. 29–37.

11. Song, Gangbing, et al.: Application of Shape Memory Alloy Wire Actuator for Precision Position Control of a Composite Beam. J. Mater. Eng. Perform., vol. 9, no. 3, pp. 330–333.

12. Shu, Steven G., et al.: Modeling of a Flexible Beam Actuated By Shape Memory Alloy Wires. Smart Mater. Struct., vol. 6, no. 3, 1997, pp. 265–277.

13. Hebda, Derek A.; and White, Scott R.: Structural Behavior of SMA Composite Beams. Proceedings of the 1995 Joint ASME Applied Mechanics and Materials Summer Meeting, vol. 206, 1995, pp. 111–119.

14. Duerig, T.W.; Melton, K.N.; and Stockel, D.: Engineering Aspects of Shape Memory Alloys. Butterworth-Heinemann, London, 1990.

15. Paine, J.S.N.; and Rogers, C.A.: Review of Multi-Functional SMA Hybrid Composites Materials and Their Applications. Adaptive Structures and Composite Materials: Analysis and Application, vol. 54, 1994, pp. 37–45.

16. Xu, Y., et al.: A New Method for Fabricating SMA/CFRP Smart Hybrid Composites. Intermetallics, vol. 10, no. 4, 2002, pp. 361–369.

17. Jang, Byung-Koog; and Kishi, Teruo: Thermomechanical Response of TiNi Fiber-Impregnated CFRP Composites. Mater. Lett., vol. 59, nos. 19–20, 2005, pp. 2472–2475.

18. ASTM D5528–13: Standard Test Method for Mode I Interlaminar Fracture Toughness of Unidirectional Fiber-Reinforced Polymer Matrix Composites. ASTM International, West Conshohocken, PA, 2013.

19. Hexcel Composites: Hexply 8552 Material Safety Data Sheet. April 1, 2009. https://shedapps.grc.nasa.gov/pdf/MSDS2010/grc-5038a-462.pdf Accessed June 15, 2018.

20. Henkel Corporation: Loctite EA 9696 15UNS AERO. Safety Data Sheet Item No. AF9118512, 2015. http://hybris.cms.henkel.com/henkel/msdspdf?matnr=698917&country=US&language=EN Accessed May 2015.
21. Cytec Engineered Materials: FM 377U Adhesive Film. Technical Data Sheet ID No. AEAD–00014, April 7, 2010. http://www.cytec.com/sites/default/files/datasheets/FM_377_040710.pdf Accessed May 2015.
22. 3M Scotch-Weld: Structural Adhesive Film AF 163–2. Nov. 2009. http://multimedia.3m.com/mws/media/282041O/3m-scotch-weld-structural-adhesive-film-af-163-2-af-163-3.pdf Accessed May 2015.
23. O'Brien, T; and Martin, R.: Round Robin Testing for Mode I Interlaminar Fracture Toughness of Composite Materials. J. Compos. Tech. Res., vol. 15, no. 4, 1993, pp. 269–281.
24. Czabaj, Michael W.; and Ratcliffe, James G.: Comparison of Intralaminar and Interlaminar Mode I Fracture Toughnesses of a Unidirectional IM7/8552 Carbon/Epoxy Composite. Compos. Sci. Technol., vol. 89, 2013, pp. 15–23.
25. Hansen, Peter; and Martin, R: DCB, 4ENF and MMB Characterisation of S2/8552 and IM7/8552. Technical Report N68171–98–M–5177. Materials Engineering Research Laboratory Ltd. (MERL), Hertford, England, 1999.
26. Schön, Joakim, et al.: A Numerical and Experimental Investigation of Delamination Behaviour in the DCB Specimen. Compos. Sci. Technol., vol. 60, no. 2, 2000, pp. 173–184.
27. Murri, Gretchen B.: Evaluation of Delamination Onset and Growth Characterization Methods Under Mode I Fatigue Loading. NASA/TM—2013-217966, 2013. http://ntrs.nasa.gov
28. De Charentenay, F.X., et al.: Characterizing the Effect of Delamination Defect by Mode I Delamination Test. Effects of Defects in Composite Materials, ASTM STP–836, 1984, pp. 84–103.
29. Johnson, W.; and Mangalgiri, P.: Investigation of Fiber Bridging in Double Cantilever Beam Specimens. J. Compos. Tech. Res., vol. 9, no. 1, 1987, pp. 10–13.
30. Tamuzs, V.; Tarasovs, S.; and Vilks, U.: Progressive Delamination and Fiber Bridging Modeling in Double Cantilever Beam Composite Specimens. Eng. Fract. Mech., vol. 68, no. 5, 2001, pp. 513–525.
31. Zok, F.; and Hom, C.L.: Large Scale Bridging in Brittle Matrix Composites. Acta Metall. Mater., vol. 38, no. 10, 1990, pp. 1895–1904.
32. Spearing, S.M.; and Evans, A.G.: The Role of Fiber Bridging in the Delamination Resistance of Fiber-Reinforced Composites. Acta Metall. Mater., vol. 40, no. 9, 1992, pp. 2191–2199.
33. Daridon, L.; Cochelin, B.; and Ferry, M. Potier: Delamination and Fiber Bridging Modeling in Composite Samples. J. Compos. Mater., vol. 31, no. 9, 1997, pp. 874–888.
34. de Groot, Peter J.; Wijnen, Peter A.M.; and Janssen, Roger B.F.: Real-Time Frequency Determination of Acoustic Emission for Different Fracture Mechanisms in Carbon/Epoxy Composites. Compos. Sci. Technol., vol. 55, no. 4, 1995, pp. 405–412.
35. Gutkin, R., et al.: On Acoustic Emission for Failure Investigation in CFRP: Pattern Recognition and Peak Frequency Analyses. Mech. Syst. Signal Process., vol. 25, no. 4, 2011, pp. 1393–1407.
36. Arumugam, V.; Sajith, S.; and Stanley, A. Joseph: Acoustic Emission Characterization of Failure Modes in GFRP Laminates Under Mode I Delamination. J. Nondestruct. Eval., vol. 30, no. 3, 2011, pp. 213–219.
37. Ramirez-Jimenez, C.R., et al.: Identification of Failure Modes in Glass/Polypropylene Composites by Means of the Primary Frequency Content of the Acoustic Emission Event. Compos. Sci. Technol., vol. 64, no. 12, 2004, pp. 1819–1827.